PAPER

Irradiation studies on a reactor pressure vessel steel using Fe^{+} ion

View the article online for updates and enhancements.

IOP ebooks™

Bringing you innovative digital publishing with leading voices to create your essential collection of books in STEM research.

Start exploring the collection - download the first chapter of every title for free.

Materials Research Express

PAPER

Irradiation studies on a reactor pressure vessel steel using Fe$^+$ ion

A Kedharnath[1,2] , **Apu Sarkar**[1,2], **Rajeev Kapoor**[1,2], **S Balaji**[3], **C David**[3], **Dhanadeep Dutta**[4], **S K Sharma**[2,4], **G Bharat Reddy**[1,2], **Saurav Sunil**[1,2], **Arnomitra Chatterjee**[1], **Harish Kumar**[5] and **Khushahal Thool**[6]

[1]   Mechanical Metallurgy Division, Bhabha Atomic Research Centre, Mumbai, 400085, India
[2]   Homi Bhabha National Institute, Mumbai, 400094, India
[3]   Materials Science Group, Indira Gandhi Centre for Atomic Research, Kalpakkam, 603102, India
[4]   Radiochemistry Division, Bhabha Atomic Research Centre, Mumbai, 400085, India
[5]   Advanced Light Water Reactor Division, Bhabha Atomic Research Centre, Mumbai, 400085, India
[6]   Department of Metallurgical Engineering and Materials Science, Indian Institute of Technology, Mumbai, 400076, India

E-mail: kedharnath@barc.gov.in

Abstract

Reactor pressure vessel steel samples were irradiated to three different doses 10, 25 and 50 displacements per atom (dpa) at 300 °C (reactor operating temperature) with 1.76 MeV Fe$^+$ ion and at the dose rate of $\sim$4.4 $\times$ 10^{-3} dpa s^{-1}. Samples were examined by Electron Backscatter Diffraction (EBSD), Grazing Incidence x-ray Diffraction (GIXRD), depth dependent Doppler Broadening Spectroscopy (DBS) and nanoindentation before and after irradiation. EBSD showed an increase in local misorientation values suggesting an increase in geometrically necessary dislocation density. GIXRD showed an increase in overall dislocation density after irradiation. DBS results suggested a non-uniform vacancy-depth distribution with the highest damage at a depth ($\sim$500 nm) which was consistent with the values from the Stopping and Range of Ions in Matter (SRIM) calculations. The mechanical response after irradiation was measured using nanoindentation. The nanohardness of the irradiated samples was higher than that of the unirradiated one and increased with the increase in dpa. GIXRD result showed that the dislocation density of 50 dpa irradiated sample was almost twice that of the unirradiated sample.

1. Introduction

The reactor pressure vessel (RPV) is the key component in light water type nuclear reactors. The RPV contains the entire reactor core and core shroud, and is also the ultimate barrier to nuclear radiation. Thus, the structural integrity of the RPV is of extreme importance for the safety and longevity of nuclear power plants. Low alloy steels with less amount of alloying content are popularly used to fabricate the RPV. 20MnMoNi55 is an Mn-Mo-Ni type low alloy steel, equivalent to SA508 Grade 3 class 1 steel. It has been used for nuclear RPVs, steam generators and compressors application for decades [1–3]. Although this steel exhibits good impact, fatigue and creep behavior [4–6], its mechanical properties degrade due to irradiation in the reactor environment [3, 7–9]. Irradiation embrittlement in considered to be the primary life limiting degradation factor of the RPV steel. Impact toughness of the steel decreases and the ductile to brittle transition temperature increases due to irradiation. These degradations of mechanical properties are linked to the microstructural modification of the steel as a result of radiation damage. Thus, it is important to understand the changes in the microstructure of RPV steel after irradiation in order to reliably predict the degradation in its mechanical properties.

Previously several irradiation experiments have been carried out with neutron, proton and heavy ions at different temperatures on different grades of RPV steels [7–19]. Wang *et al* observed interstitial dislocation loops in Chinese domestic A508-3 steel irradiated with protons at room temperature [20]. Xiao Hong *et al* observed an increase in dislocation loop size but a decrease in hardness and loop number density in proton irradiated A508-3 steel where the irradiation temperature increased from room temperature to 290 °C [21]. Jing *et al* observed an increase in nanohardness with the increase in dose in proton irradiated A508-3 steel [22]. Phythian and English

[23] showed the importance of dislocations in the clustering of defects and segregation of elements. From this they reasoned that dislocation pinning could be a possible cause of the increased hardening and embrittlement due to irradiation. Due to extensive studies, there is now a reasonable understanding of the radiation damage behavior of the RPV steel. However, most of the previous studies were focused on characterizing the microstructure at a particular length scale. It is known that irradiation of materials with ions produces a distribution of defects varying with depth, and thus the characterization of defects at different depths requires different characterization techniques.

In the present study, Fe^+ ions were used to irradiate RPV steel samples at 300 °C (the reactor operating temperature). The focus of this study was to examine the variation of dislocation and point defect densities in the materials irradiated to different displacement damage. To do so, the irradiated steel samples were characterized and examined by Electron Backscatter Diffraction (EBSD), Positron annihilation Doppler Broadening Spectroscopy (DBS), Nanoindentation and Grazing Incidence x-ray Diffraction (GIXRD). For each of the three different displacement damage levels samples, EBSD characterization was carried out on the same area of the sample before and after ion-irradiation.

2. Experimental methods

2.1. Material and samples

The material used in the present investigation is an Mn-Mo-Ni low alloy RPV steel with the chemical composition shown in table 1. Samples of dimensions $15 \times 15 \times 100$ mm^3 were cut from a forged and heat treated (normalized) block and subjected to quenching and tempering heat treatment cycle. The critical transition temperatures (A_1 and A_3) were measured by dilatometry using small cylindrical samples ($\phi 4$ mm $\times$ 10 mm) with a heating rate of 5 °C min^{-1}. The A_1 and A_3 temperatures were determined as 726 and 817 °C respectively. Quenching and tempering process was carried out in a small resistance furnace. During the heat treatment, samples were austenitized at 875 °C for 5 h then air cooled (to simulate the near surface location of thick forging) and then tempered at 650 °C for 7 h.

2.2. Self-ion irradiation

Samples were cut from the heat-treated steel block and mechanically polished to 0.5 mm thickness and subsequently electropolished in a solution of 20 ml perchloric acid and 80 ml methanol at −25 °C and 20 V. Markings were made on the steel samples after polishing using Vickers microhardness machine. The polished steel samples were subject to Fe^+ irradiation using a 1.7 MV Tandetron accelerator at Indira Gandhi Centre for Atomic Research (IGCAR), Kalpakkam, India, with 1.76 MeV energy and 12 mm beam diameter. The average ion current used was in the range of 188–239 nA, with a dose rate of $(4.6 \pm 0.2) \times 10^{-3}$ dpa s^{-1}. The irradiation was carried out in vacuum at 300 °C so as to simulate the temperature experienced in the reactor. The sample was heated by two heaters. The temperature was measured by a thermocouple and thermal camera and its feedback was used to maintain the sample in thermal equilibrium with the heater. During the measurement of beam current using the Faraday cup [24–27] the variation in the sample temperature was within 1%. Irradiation damage of 10, 25 and 50 dpa was achieved on three samples. It should be mentioned here that as the starting RPV steel was received in the tempered condition (650 °C for 7 h) it is highly unlikely that exposure at 300 °C will change the starting microstructure [28, 29].
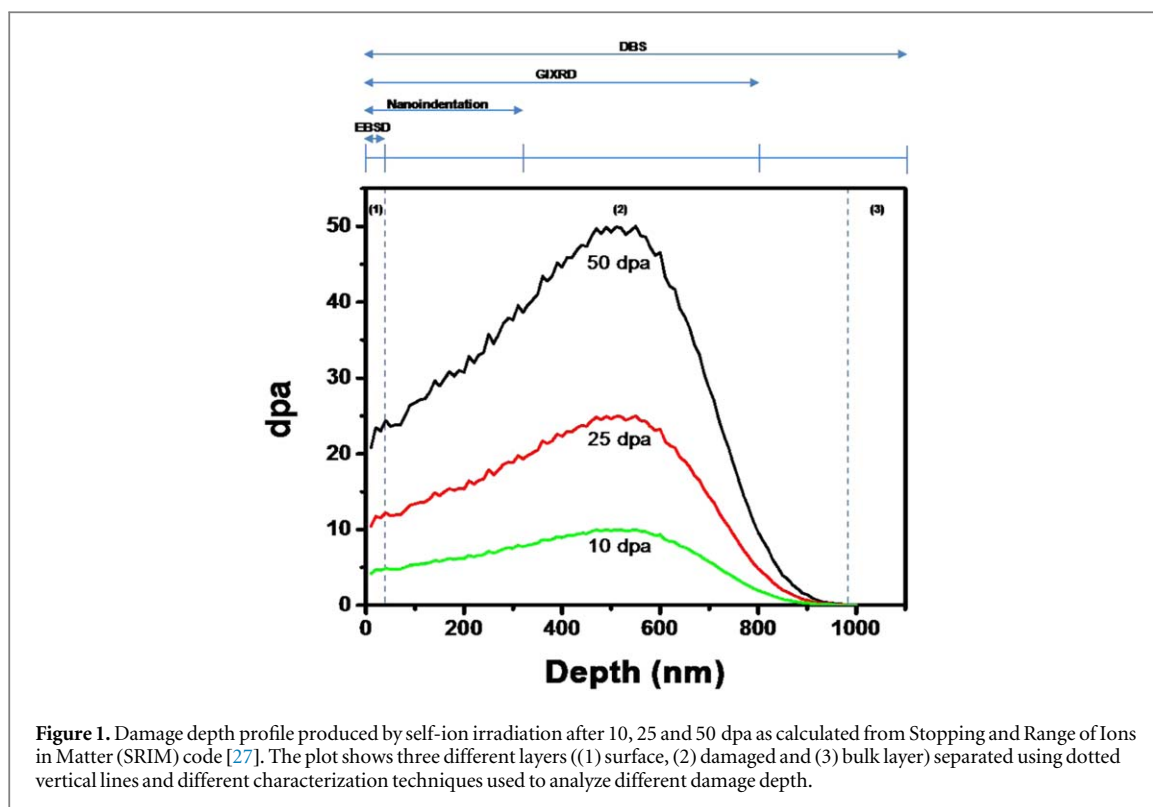
2.3. EBSD analysis

The EBSD measurements were performed on the same area of the sample before and after irradiation. EBSD was carried out on a ZEISS FEG SEM with an OXFORD HKL analysis system using an accelerating voltage of 20 kV with a step size of 0.2 μm. Micro-markings made using Vickers microhardness machine were used to locate the same area before and after irradiation for EBSD scans. Inverse pole figure (IPF) map was generated parallel to the irradiation beam direction (i.e. normal to sample surface).

2.4. Grazing incidence x-ray diffraction

The shape and broadening of the peaks in the x-ray diffraction (XRD) profile of a polycrystalline sample are sensitive to microstructural parameters like domain sizes and micro-strain developed due to the presence of crystalline defects [30, 31]. Thus, quantitative information about the microstructure of a polycrystalline sample can be estimated from the analysis of the XRD peak profile [32]. XRD line profile analyses have been extensively used to assess the microstructural changes in a variety of irradiated materials [16–19, 32–36]. Conventional XRD is suitable for investigation of the samples irradiated with neutron and proton where the damage layer extended to at least several micrometers. However, in case of the present study, the damage range is only up to 800 nm from the sample surface, as was calculated by the Stopping and Range of Ions in Matter (SRIM) code [37] as will

Table 1. Chemical composition in wt% of the low alloy steel used in this study.

C	Mn	Mo	Ni	Cr	Si	P	S	V	Al	Fe
0.16–0.20	1.20–1.50	0.40–0.55	0.50–1.00	0.15 max	0.15–0.40	0.012 max	0.008 max	0.02 max	0.01–0.04	Bal.

Figure 1. Damage depth profile produced by self-ion irradiation after 10, 25 and 50 dpa as calculated from Stopping and Range of Ions in Matter (SRIM) code [27]. The plot shows three different layers ((1) surface, (2) damaged and (3) bulk layer) separated using dotted vertical lines and different characterization techniques used to analyze different damage depth.

be shown later. To obtain the XRD profile from the near surface region, grazing incidence XRD (GIXRD) experiments were performed on the unirradiated and irradiated samples using CuK_{α} radiation at an incidence angle (ω) of $1°$. The estimated depth (t $= (\sin\omega)/\mu$, μ being the linear absorption coefficient of CuK_{α} x-ray in Fe) of penetration of x-ray during GIXRD measurements was $\sim$800 nm. The value of μ is 2405 cm^{-1} [38, 39].

2.5. Positron annihilation DBS analysis

Depth dependent Doppler broadening measurements were carried out on unirradiated and irradiated samples using a slow positron beam. Details of this set up can be found elsewhere [36]. The incident energy (E) of the positron is varied by floating the sample at requisite voltage. The total counts in each spectrum were $\sim$2 $\times$ 10^5. The Doppler broadened spectra were analyzed through line shape parameters *viz. S* and *W* parameters which signify the annihilation contribution of low momentum (valence) and high momentum (core) electrons, respectively. The *S*-parameter is calculated as the fractional area in the central region (511 $\pm$ 1.53 keV) whereas *W*-parameter is calculated as the fractional area under 4.416 keV $\leqslant$ |E$_\gamma$−511 keV| $\leqslant$ 5.761 keV energy window in the wing region of Doppler broadened annihilation peak, where E$_\gamma$ is the energy of annihilation gamma photons.
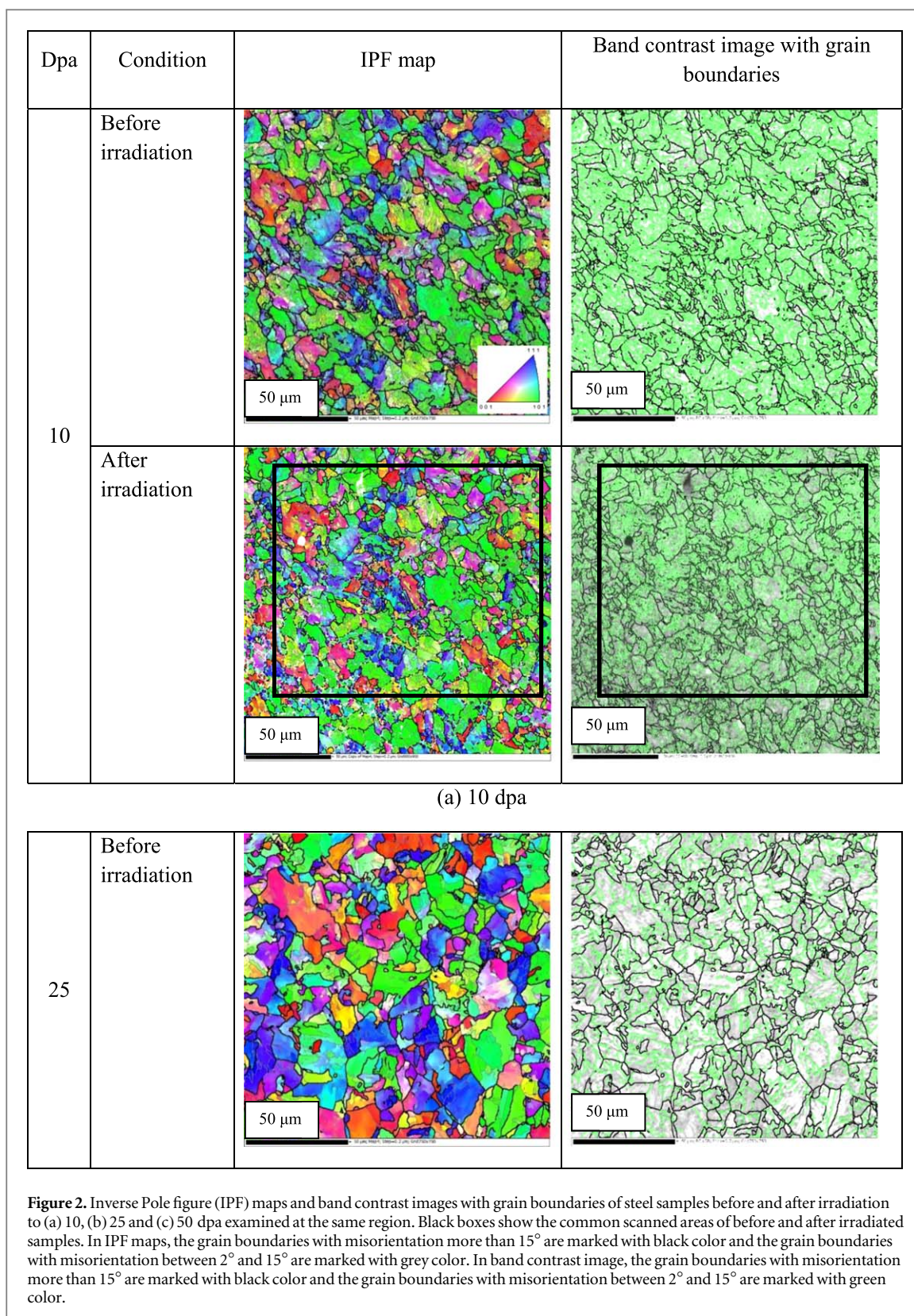
2.6. Nanoindentation

The mechanical behavior and hardness of the damage volume due to irradiation was carried out in ultra-nanohardness tester (UNHT), CSM, Switzerland with Berkovich diamond indenter. The samples were loaded to a maximum load of 5 mN with a loading rate of 1.5 mN min^{-1}. The hardness was determined using Oliver-Pharr method [40].

3. Results and discussions

3.1. SRIM calculation

The damage depth profiles were calculated using SRIM code. Calculations were made using Kinchin Pease method. Displacement energy of 40 eV was used in the SRIM calculation. The different damage profiles are identified by their maximum damage of 10, 25 and 50 dpa in the individual profile. The surface and near surface areas were less damaged compared to the peak damaged area at around 500 nm as seen in figure 1. In figure 1, three different layers were marked and separated using dotted vertical lines—(1) surface, (2) damaged and (3) bulk layer. EBSD analysis corresponds to 10–30 nm damage depth. The maximum damage depth is well beneath the area from where backscattered electrons were analyzed. Nanoindentation was carried out upto a damage depth of 150–300 nm. The estimated x-ray depth during GIXRD was 800 nm. However, the depth dependent DBS measurements have been carried out up to the bulk layer of the samples.

Dpa	Condition	IPF map	Band contrast image with grain boundaries
10	Before irradiation		
	After irradiation		

(a) 10 dpa

| 25 | Before irradiation | | |

Figure 2. Inverse Pole figure (IPF) maps and band contrast images with grain boundaries of steel samples before and after irradiation to (a) 10, (b) 25 and (c) 50 dpa examined at the same region. Black boxes show the common scanned areas of before and after irradiated samples. In IPF maps, the grain boundaries with misorientation more than 15° are marked with black color and the grain boundaries with misorientation between 2° and 15° are marked with grey color. In band contrast image, the grain boundaries with misorientation more than 15° are marked with black color and the grain boundaries with misorientation between 2° and 15° are marked with green color.
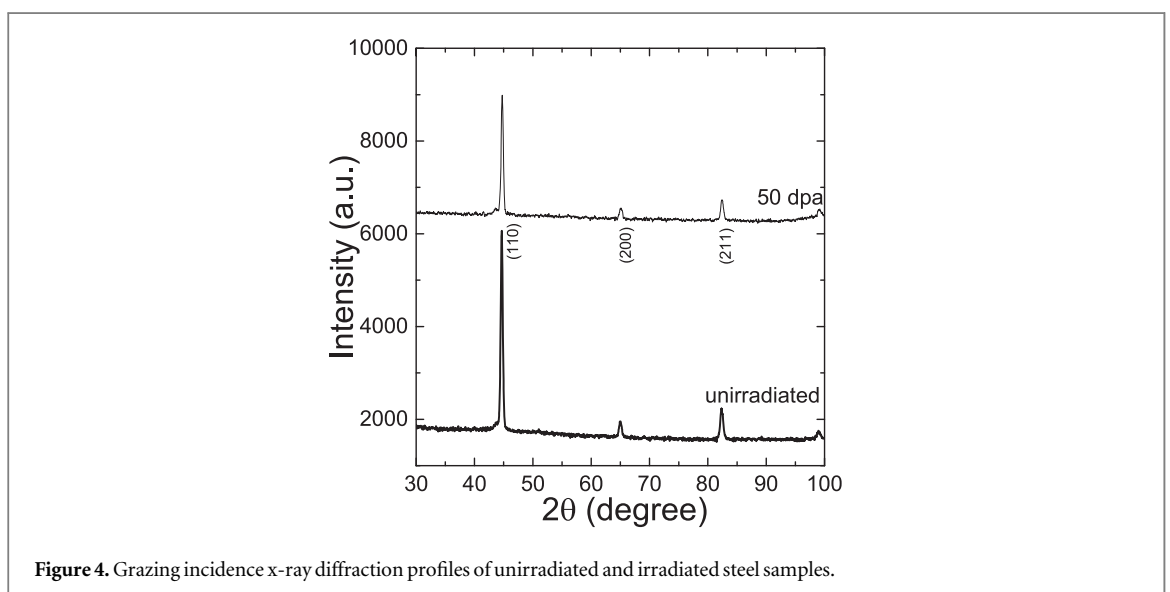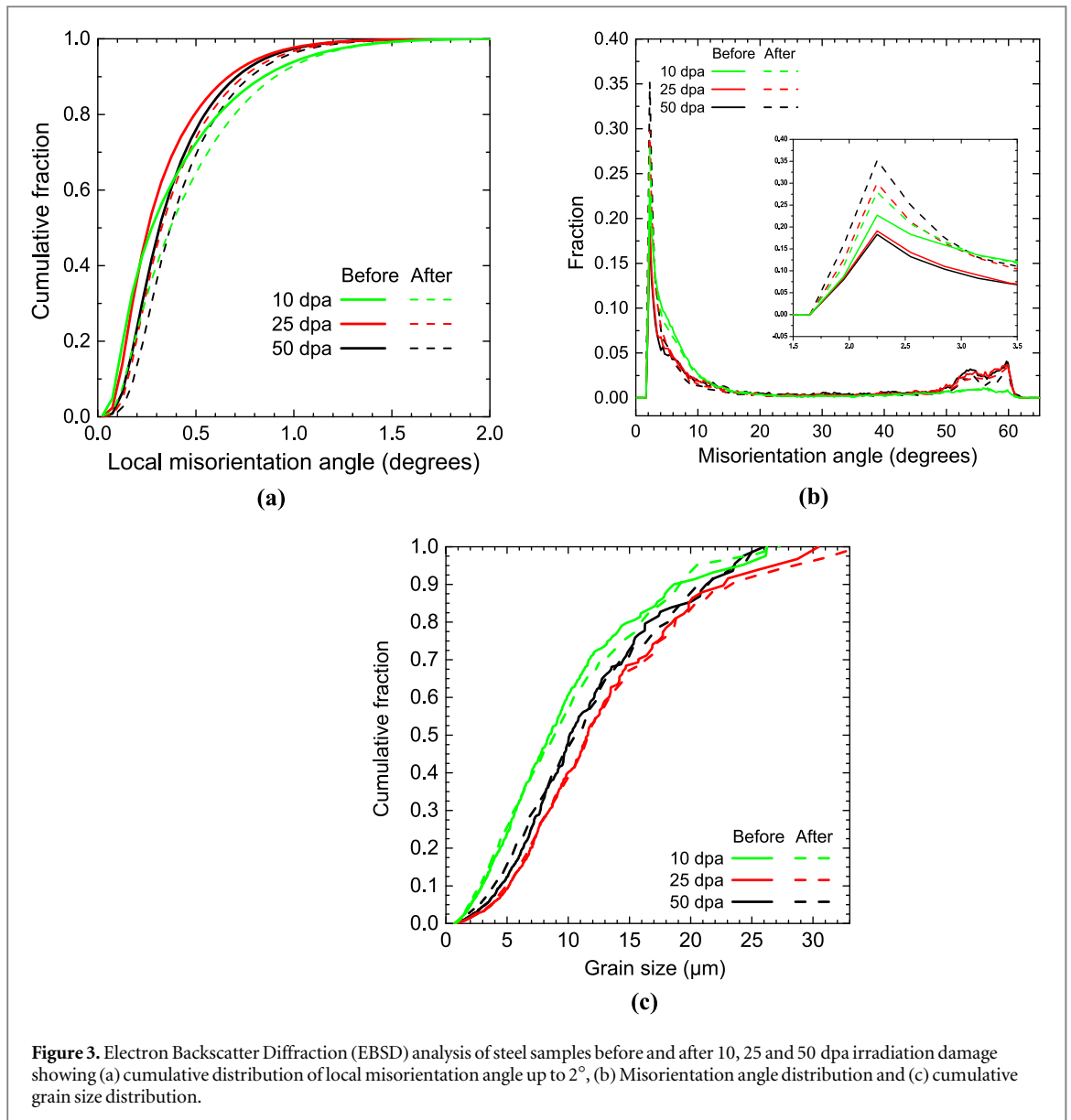
3.2. EBSD analysis

Figure 2 shows IPF map and microstructure of samples before and after irradiation carried out to different doses. It is seen that after irradiation there were no significant changes in the microstructure. Figure 3 shows plots of local misorientation, misorientation angle and grain size for samples before and after irradiation. From figure 3(a) it is seen that there was an increase in local misorientation after irradiation. This can be correlated to misorientation due to geometrically necessary dislocations (GNDs). The gradient of disorientation between the neighboring orientations gives the lattice curvature which relates to the Nye's GND density tensor. Hence the

(b) 25 dpa

(c) 50 dpa

Figure 2. (Continued.)
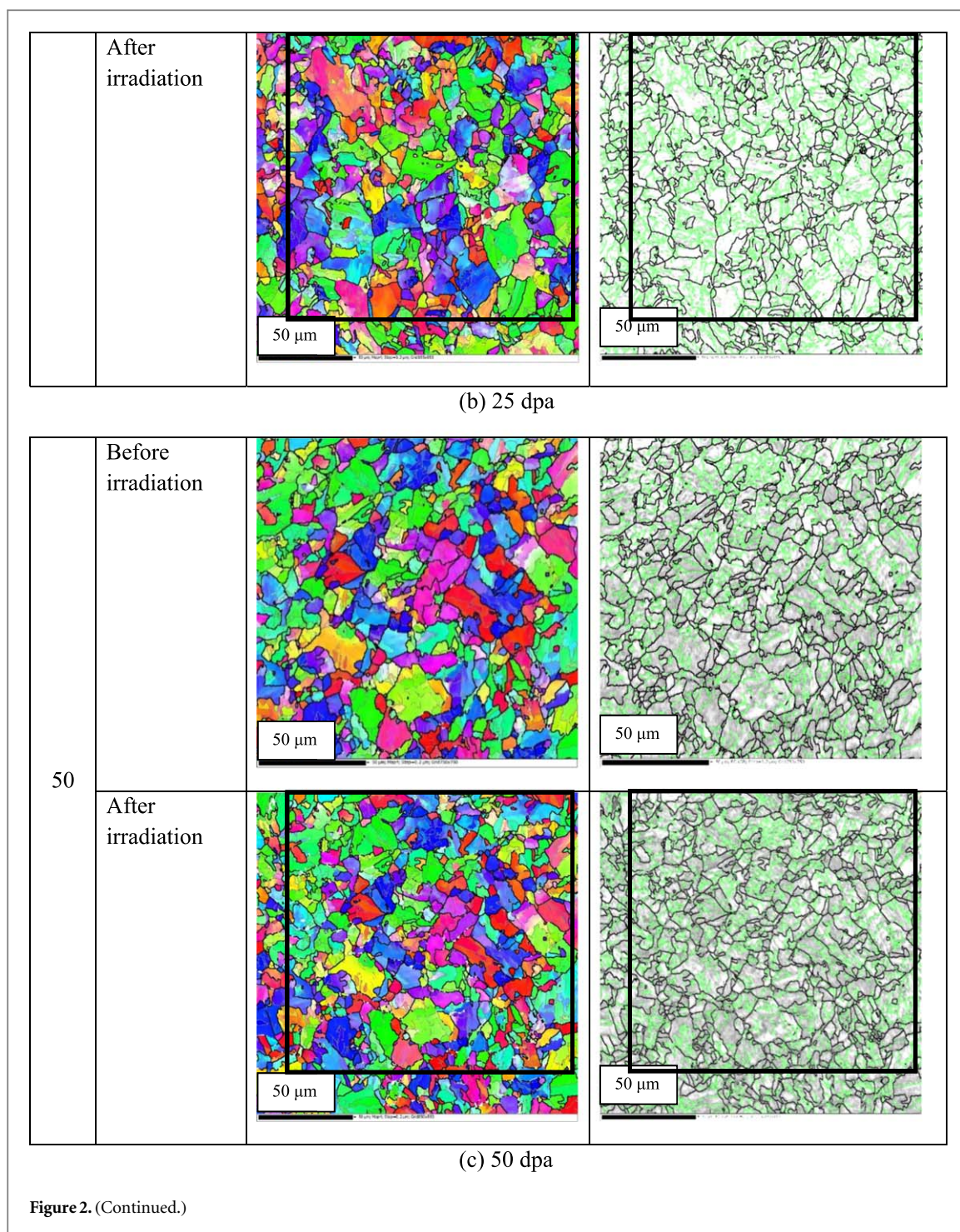
local misorientation which is the disorientation angle between the neighbor orientations can be related to GND density [41–45]. During phase transformation in bainitic steels, GNDs are formed at the bainitic interface [46]. The increase in local misorientation values in the samples after irradiation suggests an increase in GNDs. Misorientation angle distribution (figure 3(b)) shows that the fraction of low angle grain boundaries increased after irradiation. The increase was highest for the 50 dpa sample. The grain size (for grains having high angle boundaries) showed no significant change before and after irradiation (figure 3(c)). Thus, in the first 30 nm from the surface although the grain size does not change, the density of GNDs does appear to show a measurable increase.

3.3. Grazing Incidence x-ray diffraction

Figure 4 shows the GIXRD profiles of unirradiated and 50 dpa irradiated steel samples. Peaks of the GIXRD profiles were fitted with pseudo Voigt (pV) function to determine the integral breadth (β). β is essentially the
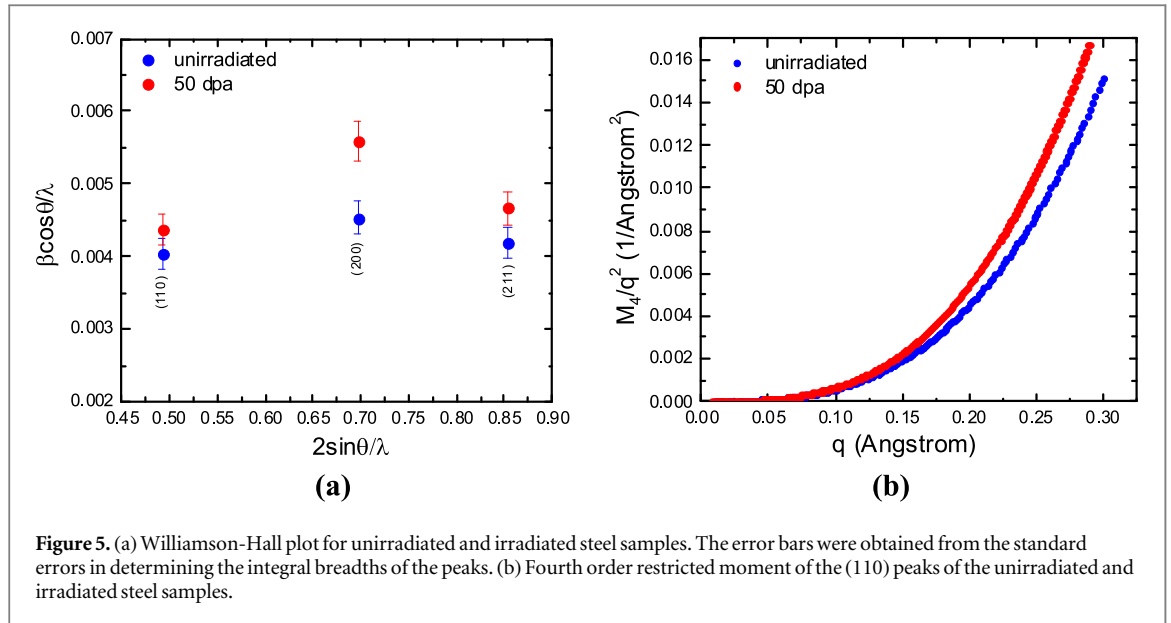
Figure 3. Electron Backscatter Diffraction (EBSD) analysis of steel samples before and after 10, 25 and 50 dpa irradiation damage showing (a) cumulative distribution of local misorientation angle up to 2°, (b) Misorientation angle distribution and (c) cumulative grain size distribution.

Figure 4. Grazing incidence x-ray diffraction profiles of unirradiated and irradiated steel samples.

Figure 5. (a) Williamson-Hall plot for unirradiated and irradiated steel samples. The error bars were obtained from the standard errors in determining the integral breadths of the peaks. (b) Fourth order restricted moment of the (110) peaks of the unirradiated and irradiated steel samples.

area of the peak divided by the peak intensity. Figure 5(a) shows the Williamson-Hall (WH) plot [47] obtained by plotting $\frac{\beta \cos \theta}{\lambda}$ against $\frac{2 \sin \theta}{\lambda}$, where θ is the Bragg angle of the peak and λ is the wavelength of the Cu K$_\alpha$ x-ray radiation. The error bars in figure 5(a) were obtained from the standard errors in determining the β. It is evident from figure 5(a) that there is an increase in broadening (β) of the peaks in the sample irradiated at a dose of 50 dpa. However, the broadening is not monotonous with 2θ, the (200) peak is broader compared to (211) peak. This type of non-monotonous broadening is termed as anisotropic broadening and is attributed to the presence of large number of dislocations in the sample. In the case of anisotropic broadening, the WH plot is not suitable to determine microstructural parameters. The variance method developed by Groma *et al* [48–51] has been shown to be appropriate for determination of the domain size and dislocation density from the anisotropically broadened XRD profile. This method is suitable for analyzing the XRD profile from a sample with inhomogeneous dislocation microstructure [49] and has been successfully utilized to characterize the irradiated sample [52, 53]. The method is based on the analysis of the moments of the intensity profile. The analytical derivation presented by Groma [49] showed that the domain size and micro-strain induced broadening influence the asymptotic behaviour of the kth-order restricted moments defined as:

$$m_k(q') = \frac{\int_{-q'}^{q'} q^k I(q) \, dq}{\int_{-\infty}^{\infty} I(q) \, dq}, \tag{1}$$

where $I(q)$ is the intensity distribution of the XRD peak, $q = 2\left(\frac{\sin \theta - \sin \theta_0}{\lambda}\right)$, θ and θ_0 are the diffraction and Bragg angle respectively. The domain size (D) and the average dislocation density (ρ) are determined from the 4th order restricted moment ($M_4(q)$) using the relation [48]:

$$\frac{M_4(q)}{q^2} = \frac{1}{3\pi^2 D} q + \frac{\Lambda \rho}{4\pi^2} + \frac{3\Lambda^2 \langle \rho^2 \rangle}{4\pi^2 q^2} \ln^2(q/q_1), \tag{2}$$

where $\langle \rho^2 \rangle$ corresponds to fluctuation is dislocation density, Λ is a geometrical constant describing the strength the dislocation contrast (with value $\sim$1) and q$_1$ is a fitting parameter.

The variance analysis was performed on the (110) peaks of the unirradiated and irradiated steel samples. Figure 5(b) shows the variation of $\frac{M_4(q)}{q^2}$ against q. The data points in the asymptotic regions were fitted with equation (2). The values of D and ρ obtained from the fitting are listed in table 2. The errors for the domain size and dislocation density values mentioned in table 2 were estimated from the standard deviation of the D and ρ values obtained from fitting different regions of the asymptotic regions of the plots in figure 5(b). The values in table 2 indicate that the domain size in the steel sample decreased after irradiation. The dislocation density in the sample irradiated up to 50 dpa is almost 2 times of that of the unirradiated sample. It is pertinent to note here that the dislocation microstructure developed in the irradiated samples was non-uniform. Dislocation density should be higher in the peak damage region i.e. $\sim$400–600 nm depth. The GIXRD profiles were recorded from a depth of 800 nm. Thus, the values of D and ρ obtained from the GIXRD peak analysis represent the average values of domain sizes and dislocation densities in the irradiated samples.

Figure 6. (a) S-E profiles of unirradiated and (b)–(d) irradiated steel samples. The solid lines through the data points show the fitting of the profiles using the program Variable Energy Positron Fit (VEPFIT).
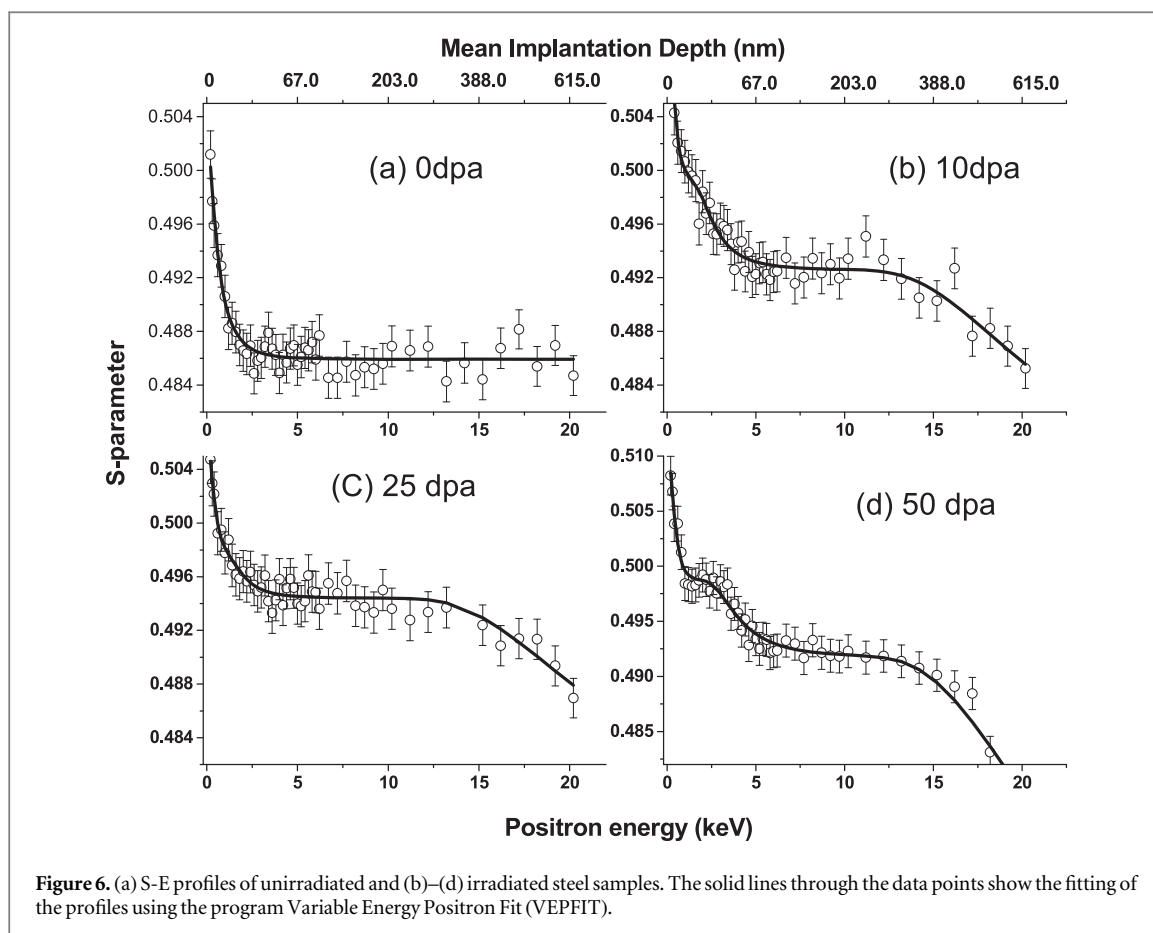
Table 2. Domain size (*D*) and average dislocation density (*ρ*) obtained from the analysis of the fourth order restricted moment. The errors for the domain size and dislocation density values were estimated from the standard deviation of the *D* and *ρ* values obtained from fitting different regions of the asymptotic regions of the plots in figure 5(b).

Sample	D (Angstrom)	$\rho\,(\mathrm{m^{-2}})$
Unirradiated	265 (±12)	$5.4\,(\pm 0.4) \times 10^{14}$
10 dpa	240 (±13)	$6.9\,(\pm 0.4) \times 10^{14}$
25 dpa	193 (±11)	$1.0\,(\pm 0.3) \times 10^{14}$
50 dpa	178 (±13)	$1.2\,(\pm 0.5) \times 10^{15}$

3.4. Positron annihilation DBS analysis

Figure 6(a) shows the *S*-parameter profiles as a function of incident positron energy (*E*) for unirradiated and irradiated steel samples with three different doses. The top axis shows the positron mean implantation depth $\langle z \rangle$ (nm) $= 40E^{1.6}/\rho_\mathrm{m}$ where *E* (keV) is the positron implantation energy and $\rho_\mathrm{m} = 7.85\ \mathrm{g\,cm^{-3}}$ is the mass density of steel. It is observed that in the case of the unirradiated sample, *S*-parameter monotonously decreases up to positron implantation energy ~3 keV and remains nearly constant at higher energies. This type of variation is typical for metallic samples. The observed higher value of S-parameter at the surface is ascribed to back diffusion of implanted positrons to the surface wherein their annihilation occurs through positronium like state. This type of *S-E* profiles indicates that the depth distribution of the defects present in the sample is uniform throughout the samples.

The *S-E* profiles in figures 6(b)–(d) of the irradiated samples are quite different from the unirradiated sample. The values of *S*-parameter remain higher as compared to unirradiated sample throughout the ion implantation depth. In the presence of open volume defects such as vacancy and vacancy-clusters, positron is trapped at the defect site due to the absence of positively charged ion cores. The relative annihilation probability of a localized positron with the surrounding valence and core electrons is reduced as compared to the

Table 3. The values of S-parameter and layer boundaries obtained from the fitting of S-E profiles using the program Variable Energy Positron Fit (VEPFIT).

Sample	$S_{surface\ layer}$	Layer boundary (nm)	$S_{damage\ layer}$	Layer boundary(nm)
10 dpa	0.4994 ± 0.0008	22.7 ± 1.8	0.4925 ± 0.0002	715.3 ± 24.2
25 dpa	0.4977 ± 0.0002	14.4 ± 2.8	0.4943 ± 0.0002	730.0 ± 26.6
50 dpa	0.4986 ± 0.0004	46.1 ± 2.8	0.4916 ± 0.0002	777.5 ± 13.6

annihilation from the delocalized state. However, the reduction in annihilation probability with core electrons (high momentum) is much higher compared to the valence electrons (low momentum). As a result, the annihilation peak is narrowed in the low momentum (central) region leading to an increase (decrease) in S-(W-) parameter. Hence, the observed higher *S*-parameter indicates that new vacancy defects are created in the samples due to irradiation. However, the *S*-parameter in the ion implanted samples begins to decrease again beyond positron incident energy ∼15 keV. This indicates that the defect depth distribution in these samples is not uniform and vacancy defect concentration is lower beyond ∼15 keV of positron implantation energy that corresponds to mean implantation depth ∼400 nm. This observation is quite consistent with the SRIM calculations as shown in figure 1. Figure 1 shows that the range of defects formation as a result of ion irradiation is up to ∼800 nm, however, their concentration is maximum at depth ∼500 nm. Interestingly, the *S-E* profiles of 50 dpa sample shows a small hump at ∼3 keV implantation energy (∼30 nm mean implantation depth) which may be attributed to the formation of large vacancy clusters or the segregation of a particular element of the RVP steel alloy (solute-enriched cluster) at the surface at higher damage [54–56].

The positron implantation profile follows the Makhovian profile that becomes broader with the increase in positron implantation energy and hence, the experimental *S*-parameter value at any depth is convoluted with the implantation profile. In the case of non-uniform depth distribution of defects, a sample can be considered as formed of multi-layers with different defect characteristics [56]. In such a case, the experimental *S*-parameter at particular implantation energy, *S*(*E*), can be defined according to equation (3), where $S_{surface}$ and S_i are the *S*-parameter values at surface and *i*th layer respectively, whereas $f_{surface}$ and f_i are the fractions of positrons annihilating from the respective surface as well as *i*th layer.

$$S(E) = S_{surface} f_{surface} + \sum_{i=1}^{k} S_i f_i \tag{3}$$

In order to extract the characteristic *S*-parameter of the damaged layer as well as the layer boundaries, the experimental *S-E* profiles have been fitted using a program Variable Energy Positron Fit (VEPFIT) [57, 58]. The solid lines through the data points in figure 6 show the fitting of the data using VEPFIT. For fitting the *S-E* profile of the unirradiated sample, a single layer has been considered. The evaluated *S*-parameter and diffusion length of positron in the unirradiated sample are 0.4859 ± 0.0001 and 6.9 ± 1.4 nm, respectively. The evaluated diffusion length (6.9 nm) in the unirradiated steel is shorter as compared to defect free metals (150–200 nm) indicating that some vacancy defects pre-exist in the steel sample. However, the fitting of the data using a single layer indicates that the pre-existing defects are distributed uniformly throughout the depth. The *S-E* profiles of the irradiated steel samples on the other hand, could not be fitted well considering single or two layers, indicating a non-uniform defect depth distribution in these samples. Importantly, a three-layer fitting could reproduce the experimental profiles of the irradiated samples. The existence of three layers in the sample is supported by the SRIM results (figure 1), where three layers can be clearly identified as surface layer, damaged layer and the bulk (undamaged) layer.

In the case of multilayer fitting using VEPFIT, a large number of free parameters are involved. It is a well-known fact that the value of positron diffusion length decreases with the increase in the defect density as positron gets trapped in the defect. Hence, the values of positron diffusion length corresponding to surface and damaged layers have been fixed at a shorter value (5 nm) as compared to the unirradiated steel sample [49]. The extracted results from the fitting are shown in table 3.

The *S*-parameter value at the surface layer (20–40 nm) is sensitive to spurious surface artifacts (sputtering due to ion irradiation, surface defects as well as oxide formation etc) and hence do not carry any significant information about the surface defects. Table 3 shows that the damaged layer is extended to ∼700–800 nm in irradiated steel samples consistent with the SRIM results. Although, the evaluated *S*-parameter corresponding to damaged layer for all the irradiated steel samples is higher than the unirradiated one (0.4859), there is no significant variation in *S*-parameter among the irradiated steel samples with the irradiation dose. It is possible that open volume defect density is very high in 10 dpa irradiated steel sample which leads to saturation trapping of positron in the sample. In such a case, even the defect density would increase beyond 10 dpa, positron annihilation characteristics (*S*-parameter) will not be sensitive to that change in the defect density. Another
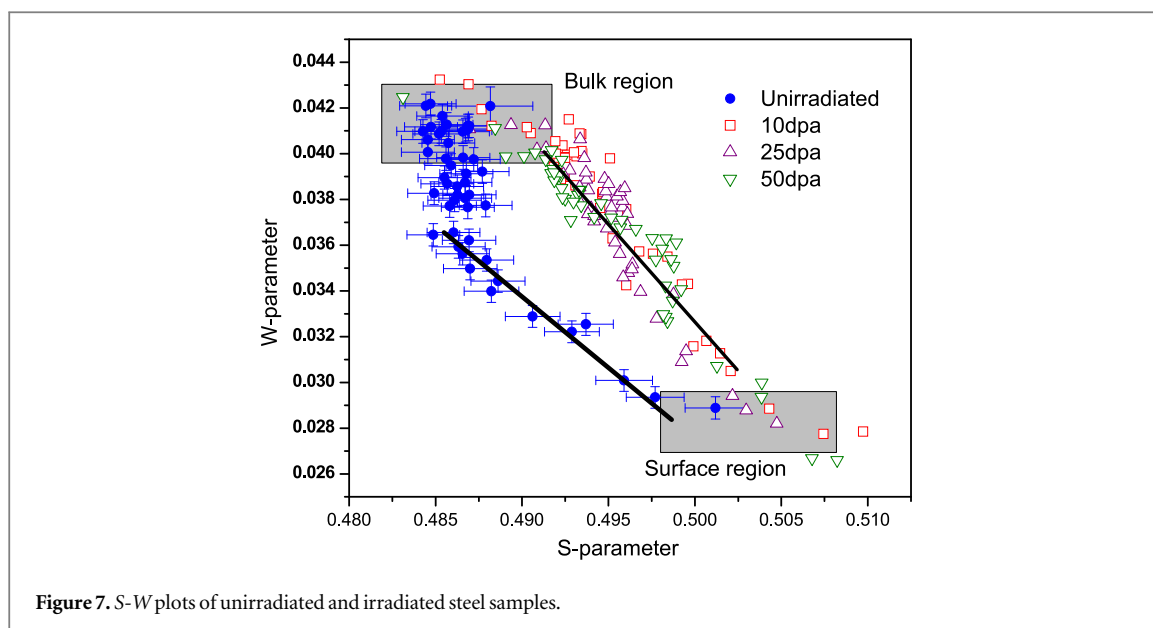
Figure 7. *S-W* plots of unirradiated and irradiated steel samples.

possible reason for not observing any variation in *S*-parameter with the increase in dose can be occupation of vacancy defects by the implanted Fe ions.

In order to identify the type of the defects created by Fe^+ ion irradiation, *S-W* plots have been drawn keeping positron implantation energy as running parameters as shown in figure 7. The data points of all the irradiated steel samples follow a single trend indicating that there is no change in the type of defects as a function of dose [49]. The *S-W* curves for unirradiated and irradiated samples follow nearly parallel lines indicating that the size of defects in these samples are the same whereas the concentration of the defects in irradiated samples has increased.

3.5. Nanoindentation

Figure 8 shows load-depth (*p-h*) behavior of unirradiated and irradiated steel samples and variation of hardness as a function of dose (dpa). Figure 8(a) shows that for constant applied load, the depth of the indenter decreased with increasing dpa signifying irradiation hardening. The indenter depth for unirradiated steel sample was twice the 50 dpa irradiated steel sample showing that hardness doubled after irradiating the sample to 50 dpa. The stiffness during loading was highest for 50 dpa irradiated steel sample. The irradiated steel samples had almost similar slope during loading. Unirradiated material showed elastic relaxation after unloading from 310 nm to 275 nm while irradiated steel samples showed negligible elastic relaxation. This can be due to locking of dislocations in the irradiated steel samples. 50 dpa irradiated steel sample showed higher resistance to indentation suggesting the highest hardness. This can be due to the irradiation induced defects like defect clusters, dislocation loops and elemental segregation.

4. Summary and conclusion

Irradiation damage in bainitic steel was quantified using four different techniques which probe different depths of the irradiated samples. The characterization of defects was carried out using EBSD, GIXRD and DBS measurements while mechanical characterization was carried out using nanoindentation. EBSD measurements, which quantify the damage of about 30 nm from the surface, showed that though there was no change in grain size there was an increase in GNDs after irradiation. As EBSD measurements give information about only GNDs from near to the irradiated surface, other techniques were used to quantify defects at greater depths. GIXRD was able to capture total dislocation density (both statistically stored dislocations as well as geometrically necessary dislocations) from large irradiated area and a depth of about 800 nm. From GIXRD results, it was seen that RPV steel sample irradiated to a peak of 50 dpa showed double the dislocation density as compared to that of the unirradiated sample. Recent cascade collision simulations have also shown an increase in dislocation density after irradiation [59–66]. However, as both EBSD and GIXRD measurements are not suited to capture the presence of point defects, positron annihilation DBS measurements were carried out to quantify vacancies at different depths from the irradiated surface. Vacancy depth distribution was not uniform. S-E profile analyses suggest elemental segregation (solute enriched cluster) in 50 dpa irradiated sample. S-W plot showed that there was no change in the type and size of the defect, but irradiated samples had a higher concentration of vacancies than the unirradiated sample. Correlating the increase in defects (both vacancy concentration and dislocation
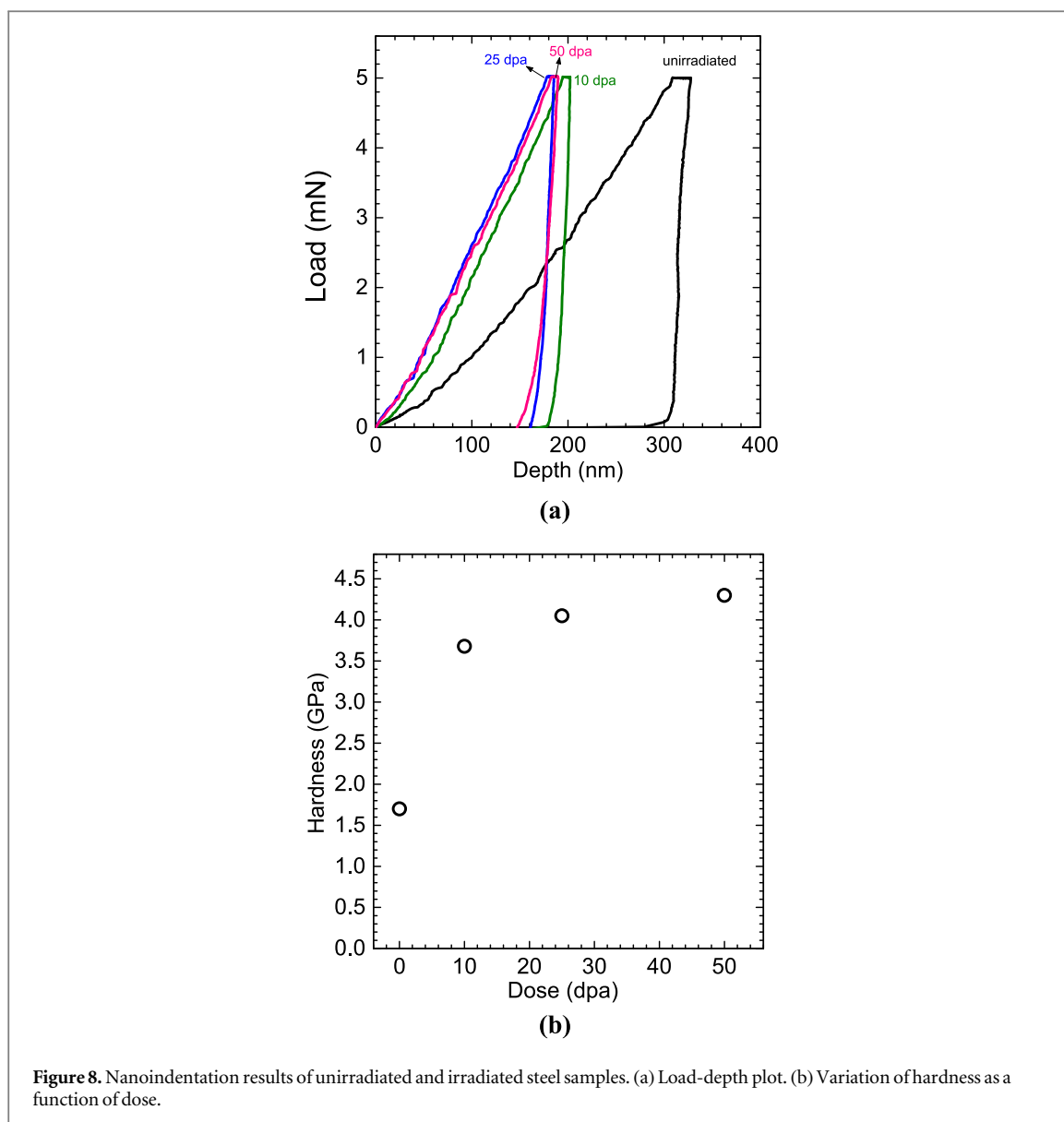
Figure 8. Nanoindentation results of unirradiated and irradiated steel samples. (a) Load-depth plot. (b) Variation of hardness as a function of dose.

density) to the hardening behavior of the material, nanoindentation results showed an increase in hardness for irradiated samples. Nanoindentation was able to capture the effect of increase in dislocation density and defect concentration in the irradiated samples. Higher dpa samples showed higher hardness values supporting EBSD and GIXRD results.

Due to the technical importance of RPV steels, several irradiation studies using various ion species have been carried out on them. Most of the studies were aimed to identify the reason of embrittlement in RPV steel due to irradiation. Previous investigation using transmission electron microscopy indicated increase in dislocation loop density in irradiated RPV [20, 67–71]. Hailong Liu did EBSD analysis on three commercial RPV steels to compare and validate GNDs values with XRD analysis [70]. Positron annihilation spectroscopy has been extensively used to characterize the irradiated RPV steel [68, 69, 72, 73]. For example, Jiang *et al* [54], Shi *et al* [73] and Liu *et al* [74] observed an increase in vacancy type defects, vacancy clusters and vacancy-solute complexes in proton and ion irradiated RPV steel. Nanoindentation studies on the irradiated samples showed hardening due to irradiation induced defects such as vacancy type defects, dislocation loops and elemental segregations and clusters [68, 69]. Nanoindentation study by Jing *et al* [22] on the proton irradiated RPV steel revealed a notable increase in the nanohardness which was correlated with an increase in dislocation density and vacancy type defect. Atomistic simulations of edge [75] and screw [72] dislocations in irradiated steel showed point defects and elemental clustering near dislocations. It is seen that the previous results obtained on the irradiated RPV steels corroborate with that of the present study.

In conclusion, the microstructure of the Mn-Mo-Ni low alloy RPV steel samples irradiated using 1.76 MeV Fe^+ ion at 300 °C were characterized using different complementary techniques. EBSD and GIXRD results

indicated an increase in dislocation density due to irradiation. DBS study using positron annihilation signified irradiation induced formation of vacancy type defect in the RPV steel. At higher dose, large vacancy clusters and solute-enriched cluster were formed. Generation of these microstructural defects resulted in an increase in the nanohardness of the irradiated steel samples.

Acknowledgments

ORCID iDs

A Kedharnath ⓘ https://orcid.org/0000-0002-1517-4754

References

[1] INTERNATIONAL ATOMIC ENERGY AGENCY, Integrity of Reactor Pressure Vessels in Nuclear Power Plants: Assessment of Irradiation Embrittlement Effects in Reactor Pressure Vessel Steels, Nuclear Energy Series No. NP-T-3.11, IAEA, Vienna. 2009 (https://www.iaea.org/publications/7915/integrity-of-reactor-pressure-vessels-in-nuclear-power-plants-assessment-of-irradiation-embrittlement-effects-in-reactor-pressure-vessel-steels)

[2] Suzuki K, Kurihara I, Sasaki T, Koyoma Y and Tanaka Y 2001 Application of high strength MnMoNi steel to pressure vessels for nuclear power plant *Nucl. Eng. Des.* **206** 261–77

[3] Davies L M 1999 A comparison of Western and Eastern nuclear reactor pressure vessel steels *Int. J. Press. Vessel. Pip.* **76** 163–208

[4] Sarkar A, Bhupendra K K and Chakravartty J K 2015 Low cycle fatigue behavior of a ferritic reactor pressure vessel steel *J. Nucl. Mater.* **462** 273–9

[5] Sarkar A, Bhupendra K K and Chakravartty J K 2015 Ratchetting behavior of 20MnMoNi55 reactor pressure vessel steel *J. Nucl. Mater.* **467** 500–4

[6] Gopalan A, Samal M K and Chakravartty J K 2015 Fracture toughness evaluation of 20MnMoNi55 pressure vessel steel in the ductile to brittle transition regime: experiment & numerical simulations *J. Nucl. Mater.* **465** 424–32

[7] Jin H-H, Kwon J and Shin C 2014 Evolution of radiation defect and radiation hardening in heat treated SA508 Gr3 steel *Nucl. Instrum. Methods Phys. Res., Sect.* B **319** 24–8

[8] Suzuki K. 1982 Neutron irradiation embrittlement of ASME SA508, C1. 3 Steel *J. Nucl. Mater.* **108–109** 443–450

[9] Gurovich B, Kuleshova E, Shtrombakh Y, Fedotova S, Erak D and Zhurko D 2015 Evolution of microstructure and mechanical properties of VVER-1000 RPV steels under re-irradiation *J. Nucl. Mater.* **456** 373–81

[10] Kasada R, Takayama Y, Yabuuchi K and Kimura A 2011 A new approach to evaluate irradiation hardening of ion-irradiated ferritic alloys by nano-indentation techniques *Fusion Eng. Des.* **86** 2658–61

[11] Kishimoto H, Yutani K, Kasada R and Kimura A 2006 Helium cavity formation research on oxide dispersion strengthening (ODS) ferritic steels utilizing dual-ion irradiation facility *Fusion Eng. Des.* **81** 1045–9

[12] Heintze C, Bergner F and Hernández-Mayoral M 2011 Ion-irradiation-induced damage in Fe-Cr alloys characterized by nanoindentation *J. Nucl. Mater.* **417** 980–3

[13] Zou J X, Zhang K M, Grosdidier T, Dong C, Qin Y, Hao S Z and Yang D Z 2008 Orientation-dependent deformation on 316L stainless steel induced by high-current pulsed electron beam irradiation *Mater. Sci. Eng.* A **483–484** 302–5

[14] Xu C, Zhang L, Qian W, Mei J and Liu X 2016 The studies of irradiation hardening of stainless steel reactor internals under proton and xenon irradiation *Nucl. Eng. Technol.* **48** 758–64

[15] Takayama Y, Kasada R, Sakamoto Y, Yabuuchi K, Kimura A, Ando M, Hamaguchi D and Tanigawa H 2013 Nanoindentation hardness and its extrapolation to bulk-equivalent hardness of F82H steels after single- and dual-ion beam irradiation *J. Nucl. Mater.* **442** S23–7

[16] Alsabbagh A, Sarkar A, Miller B, Burns J, Squires L, Porter D, Cole J I and Murty K L 2014 Microstructure and mechanical behavior of neutron irradiated ultrafine grained ferritic steel *Mater. Sci. Eng.* A **615** 128–38

[17] Mukherjee P, Sarkar A and Barat P 2005 Microstructural changes in oxygen-irradiated zirconium-based alloy characterised by x-ray diffraction techniques *Mater. Charact.* **55** 412–7

[18] Sarkar A, Mukherjee P and Barat P 2008 Effect of heavy ion irradiation on microstructure of zirconium alloy characterised by x-ray diffraction *J. Nucl. Mater.* **372** 285–92

[19] Sharma G, Mukherjee P, Chatterjee A, Gayathri N, Sarkar A and Chakravartty J K 2013 Study of the effect of α irradiation on the microstructure and mechanical properties of nanocrystalline Ni *Acta Mater.* **61** 3257–66

[20] Wang R, Xu C, Liu X, Huang P and Ren A 2013 Microstructural and mechanical studies of reactor pressure vessel steel under proton irradiation *J. Alloys Compd.* **581** 788–92

[21] Li X H, Lei J, Shu G G and Wan Q M 2015 A study on the microstructure and mechanical property of proton irradiated A508-3 steel *Nucl. Instruments Methods Phys. Res. Sect. B Beam Interact. with Mater. Atoms* **350** 14–9

[22] Lei J, Ding H, Shu G G and Wan Q M 2014 Study on the mechanical properties evolution of A508-3 steel under proton irradiation *Nucl. Instruments Methods Phys. Res. Sect. B Beam Interact. with Mater. Atoms* **338** 13–8

[23] Phythian W J and English C A 1993 Microstructural evolution in reactor pressure vessel steels *J. Nucl. Mater.* **205** 162–77

[24] Suresh K *et al* 2019 Development of a dual ion irradiation facility for studies of radiation response in fission and fusion reactor materials *Nucl. Instrum. Methods Phys. Res., Sect.* B **447** 92–9

[25] Suresh K *et al* 2018 Development of a simple, low cost, indirect ion beam fluence measurement system for ion implanters, accelerators *J. Instrum.* **13** P02033

[26] David C *et al* 2008 A study of the effect of titanium on the void swelling behavior of D9 steels by ion beam simulation *J. Nucl. Mater.* **383** 132–6

[27] David C *et al* 2009 Void swelling in ion irradiated (15Ni–14Cr), Ti-modified stainless steel: a study using positron annihilation and step height measurements *Surface & Coatings Technology* **17** 2363–6

[28] Luo X, Han L and Gu J 2016 Study on austenitization kinetics of SA508 Gr. 3 steel based on isoconversional method *Metals.* **6** 8

[29] Zuna P *et al* 2012 Kinetics of Grain Growth and Recrystallization during Forming Modes for Processing of Steel SA 508 (http://metal2012.tanger.cz/files/proceedings/02/reports/389.pdf)

[30] Cullity B D 1978 *Elements of X-ray Diffraction* (Philippines: Addison-Wesley Publishing Company)

[31] Warren B E 2012 *X-Ray Diffraction* (New York: Dover Publications)

[32] Mukherjee P, Sarkar A, Barat P, Bandyopadhyay S K, Sen P, Chattopadhyay S K, Chatterjee P, Chatterjee S K and Mitra M K 2004 Deformation characteristics of rolled zirconium alloys: a study by x-ray diffraction line profile analysis *Acta Mater.* **52** 5687–96

[33] Sarkar A, Mukherjee P and Barat P 2008 Characterization of irradiated microstructure by x-ray diffraction line profile analysis *Metall. Mater. Trans. A Phys. Metall. Mater. Sci* **39** 1602–9

[34] Mukherjee P, Sarkar A, Bhattacharya M, Gayathri N and Barat P 2009 Post-irradiated microstructural characterisation of cold-worked SS316L by x-ray diffraction technique *J. Nucl. Mater.* **395** 37–44

[35] Mukherjee P, Sarkar A, Barat P, Raj B and Mudali U K 2005 Microstructural studies on lattice imperfections in irradiated titanium and Ti-5% Ta-2% Nb by x-ray diffraction line profile analysis *Metall. Mater. Trans. A* **36** 2351–60

[36] Maheshwari P, Pujari P K, Sharma S K, Sudarshan K, Dutta D, Samanta S, Singh A, Aswal D K, Ajay Kumar R and Samajdar I 2012 Defect profiling in organic semiconductor multilayers *Org. Electron. Physics, Mater. Appl* **13** 1409–19

[37] Ziegler J F, Ziegler M D and Biersack J P 2010 SRIM-the stopping and range of ions in matter (2010) *Nucl. Instruments Methods Phys. Res. Sect. B Beam Interact. with Mater. Atoms.* **268** 1818–23

[38] Saloman E B, Hubbell J H and Scofield J H 1988 X-ray attenuation cross sections for energies 100 eV to 100 keV and elements Z = 1 to Z = 92 *Atomic Data and Nuclear Data Tables* **38** 1–196

[39] Saloman E B and Hubbell J H 1986 *X-ray Attenuation Coefficients (Total Cross Sections): Comparison of the Experimental Data Base With the Recommended Values of Henke and the Theoretical Values of Scofield for Energies Between 0.1-100 keV* (Gaithersburg, MD, USA: NBS publications)

[40] Oliver G M and Pharr W C 1992 An improved technique for determing hardness and elastic modulus using load and displacement sensing indentation experiments *J. Mater. Res.* **7** 1564–83

[41] Britton T B and Hickey J L R 2018 Understanding deformation with high angular resolution electron backscatter diffraction (HR-EBSD) *IOP Conf. Series: Materials Science and Engineering* vol 304 (Bristol) (IOP Publishing)

[42] Wright S I, Field D P and Nowell M M 2015 Post processing effects on GND calculations from EBSD-based orientation measurements *IOP Conf. Series: Materials Science and Engineering* vol 89 (Bristol) (IOP Publishing)

[43] Moussa C *et al* 2015 About quantitative EBSD analysis of deformation and recovery substructures in pure tantalum *IOP Conference Series: Materials Science and Engineering* vol 89 (Bristol: IOP Publishing)

[44] Kapoor R *et al* 2010 Influence of fraction of high angle boundaries on the mechanical behavior of an ultrafine grained Al–Mg alloy *Materials Science and Engineering: A* **527** 5246–54

[45] Basu I, Ocelík V and De Hosson J T M 2017 Quantitative estimation of spatial stress gradients from dislocation pile-up at grain boundaries in commercially pure titanium *The British Society for Strain Measurement*

[46] Bhadeshia H K D H 2015 *Bainite in Steels: Theory and Practice* 3rd edition (Leeds, UK: Maney Publishing)

[47] Williamson G K and Hall W H 1953 X-ray line broadening from filed aluminium and wolfram *Acta Metall.* **1** 22–31

[48] Borbély A and Groma I 2001 Variance method for the evaluation of particle size and dislocation density from x-ray Bragg peaks *Appl. Phys. Lett.* **79** 1772–4

[49] Groma I 1998 X-ray line broadening due to an inhomogeneous dislocation distribution *Phys. Rev. B - Condens. Matter Mater. Phys.* **57** 7535–42

[50] Sarkar A, Mukherjee P and Barat P 2008 X-ray diffraction studies on asymmetrically broadened peaks of heavily deformed zirconium-based alloys *Mater. Sci. Eng. A* **485** 176–81

[51] Sarkar A, Bhowmik A and Suwas S 2009 Microstructural characterization of ultrafine-grain interstitial-free steel by x-ray diffraction line profile analysis *Appl. Phys. A Mater. Sci. Process.* **94** 943–8

[52] Bhattacharyya P *et al* 2017 Proton irradiation studies on Al and Al5083 alloy *Radiat. Phys. Chem.* **139** 132–40

[53] Gupta A D *et al* 2016 Proton irradiation studies on pure Ti and Ti-6Al-4V *Nucl. Instrum. Methods Phys. Res., Sect. B* **387** 63–72

[54] Jiang J, Wu Y C, Liu X B, Wang R S, Nagai Y, Inoue K, Shimizu Y and Toyama T 2015 Microstructural evolution of RPV steels under proton and ion irradiation studied by positron annihilation spectroscopy *J. Nucl. Mater.* **458** 326–34

[55] Zhang T, Schut H, Li Z, Wang H, Zhang Z and He M 2018 Positron annihilation and nano-indentation analysis of irradiation effects on the microstructure and hardening of A508-3 steels used in Chinese HTGR *J. Nucl. Sci. Technol.* **55** 418–23

[56] Saini S, Menon R, Sharma S K, Srivastava A P, Mukherjee S, Nabhiraj P Y, Pujari P K, Srivastava D and Dey G K 2016 Ar irradiated Cr rich Ni alloy studied using positron annihilation spectroscopy *J. Nucl. Mater.* **479** 279–86

[57] van Veen A, Schut H, Clement M, de Nijs J M M, Kruseman A and IJpma M R 1995 VEPFIT applied to depth profiling problems *Appl. Surf. Sci.* **85** 216–24

[58] van Veen A, Schut H, de Vries J, Hakvoort R A and Ijpma M R 1991 Analysis of positron profiling data by means of 'VEPFIT' *AIP Conf. Proc* **218** 171–98

[59] Sand A E, Dudarev S L and Nordlund K 2013 High-energy collision cascades in tungsten: dislocation loops structure and clustering scaling laws *EPL (Europhysics Letters)* **103** 46003

[60] Wang H *et al* 2018 Collision cascades interact with an edge dislocation in bcc Fe: a molecular dynamics study *RSC Adv.* **8** 14017–24

[61] Singh D *et al* 2019 Effect of symmetrical and asymmetrical tilt grain boundaries on the tensile deformation of zirconium bicrystals: a MD-based study *J. Mater. Sci.* **54** 3082–95

[62] Kedharnath A, Kapoor R and Sarkar A 2019 Atomistic simulation of interaction of collision cascade with different types of grain boundaries in α-Fe *J. Nucl. Mater.* **523** 444–57

[63] Fu B Q *et al* 2017 Effect of collision cascades on dislocations in tungsten: a molecular dynamics study *Nucl. Instrum. Methods Phys. Res., Sect. B* **393** 169–73

[64] Voskoboinikov R E 2013 MD simulations of collision cascades in the vicinity of a screw dislocation in aluminium *Nucl. Instrum. Methods Phys. Res., Sect. B* **303** 104–7

[65] Granberg F *et al* 2017 Cascade debris overlap mechanism of ⟨100⟩ dislocation loop formation in Fe and FeCr *Europhys. Lett.* **119** 5

[66] Singh D *et al* 2019 Molecular dynamics-based simulations to study crack tip interaction with symmetrical and asymmetrical tilt grain boundaries *J. Nucl. Mater.* 151739

[67] Chaouadi R *et al* 2019 Neutron irradiation hardening of chemically-tailored RPV steels with respect to Cu/P and Ni/Mn elements *J. Nucl. Mater.* **519** 188–204

[68] Shi J J *et al* 2019 Characterization of proton-irradiated Chinese A508-3-type reactor pressure vessel steel by slow positron beam, TEM, and nanoindentation *Nucl. Instrum. Methods Phys. Res., Sect.* B **443** 62–9

[69] Shi J J *et al* 2019 Evolution of microstructures and hardening property of initial irradiated, post-irradiation annealed and re-irradiated Chinese-type low-Cu reactor pressure vessel steel *J. Nucl. Mater.* **523** 333–41

[70] Liu H and Li Q 2019 Dislocation density evaluation of three commercial SA508Gr. 3 steels for reactor pressure vessel *IOP Conf. Series: Materials Science and Engineering* vol 490 *(Bristol)* (IOP Publishing)

[71] Liu H *et al* 2019 The microstructural characterization of NiSi-Rich sub-precipitates within cementite in isothermally aged reactor pressure vessel steel *Metallurgical and Materials Transactions* A **50** 3992–9

[72] Liu H *et al* 2019 The effect of dislocations on irradiation-induced vacancy-like defects in FeCu alloy and reactor pressure vessel steel *J. Nucl. Mater.* **524** 80–9

[73] Shi J J *et al* 2019 Slow positron beam study of highly irradiated RPV steel under proton and ion impact *Radiat. Phys. Chem.* **156** 199–204

[74] Liu X *et al* 2012 Positron annihilation study of proton-irradiated reactor pressure vessel steels *Radiat. Phys. Chem.* **81** 1586–92

[75] Wang D *et al* 2019 Effect of edge dislocation on solute-enriched clusters in reactor pressure vessel steel *Nucl. Instrum. Methods Phys. Res., Sect.* B **451** 55–60